Strain-engineered ferroelectricity in 2H bilayer MoS_2

Jianfeng Mao[1,2], Jingyu He[1], Weng Fu Io[1], Feng Guo[1,2], Zehan Wu[1,2], Ming Yang[1,3], Jianhua Hao[1,2,3]*

1 Department of Applied Physics, The Hong Kong Polytechnic University, Hung Hom, Hong Kong 999077, P. R. China

2 The Hong Kong Polytechnic University Shenzhen Research Institute, Shenzhen 518057, P. R. China

3 Research Centre for Nanoscience and Nanotechnology, The Hong Kong Polytechnic University, Hong Kong 999077, P. R. China

* Corresponding authors: jh.hao@polyu.edu.hk

KEYWORDS: MoS_2, nanocone arrays, strain engineering, piezoelectric coefficient, ferroelectricity

ABSTRACT

The exploration of two-dimensional (2D) materials exhibiting out-of-plane ferroelectric and piezoelectric properties through interlayer twist/translation or strain, known as sliding ferroelectricity, has become a focal point in the quest for low-power electronic devices, capitalizing on the weak van der Waals interactions. Herein, we delve into the behavior of

strained bilayer molybdenum disulfide (2L-MoS_2) transferred onto a nanocone-patterned substrate. A remarkable observation is the emergence of unexpected vertical ferroelectricity in MoS_2, irrespective of whether it was prepared using chemical vapor deposition or mechanically exfoliated from bulk crystal. Such observation underscores the versatility and reproducibility of the emerging ferroelectricity across different preparation methods. Furthermore, the effective piezoelectric coefficients recorded are exceptionally high, with the values of 18.77 pm V^{-1} and 12.40 pm V^{-1} for monolayer and bilayer MoS_2, respectively, outperforming most currently discovered 2D piezoelectrics. The presence of room-temperature out-of-plane ferroelectricity in strained 2L-MoS_2 is confirmed through first-principles calculations and piezoresponse force microscopy. This ferroelectric behavior can be contributed to the symmetry breaking and interlayer sliding within strained 2L-MoS_2 structure. Our findings not only deepen the understanding of ferroelectricity in 2D materials but also pave the way for designing new 2D ferroelectrics, thereby unlocking novel functionalities and promising ferroelectric applications.

1. INTRODUCTION

Two-dimensional (2D) ferroelectrics exhibit spontaneous electric polarization which is switchable under an external electric field. This unique property positions ferroelectrics as crucial components in non-volatile memory devices, transistors, and sensors[1-6]. Despite theoretical predictions of various 2D ferroelectric materials, only a limited number of materials, including SnTe[7], $CuInP_2S_6$[8], $MoTe_2$[9], α-In_2Se_3[10], and $CuCrP_2S_6$[11], have been experimentally validated thus far. This is primarily due to the requirement of a non-centrosymmetric atomic structure and spontaneous polarization along specific orientations. Extensive efforts have been dedicated to

the exploration of new 2D ferroelectric semiconductors. Li et al. proposed that vertical ferroelectricity could be achieved by artificially stacking van der Waals (vdW) bilayers with a twist angle or relative lateral shift[12]. The polarization switching in this scenario could be achieved through interlayer translation between two parallel layers, a phenomenon known as sliding ferroelectricity. Notably, this mechanism differs significantly from conventional ferroelectric switching mechanism that relies on interlayer ion displacement. Since then, experimental confirmations of such ferroelectricity have been achieved in bilayer BN[13, 14], transition-metal dichalcogenides (TMDs)[15-18], and γ-InSe[19].

On the other hand, strain engineering has proven to be a valuable tool for modifying the crystallographic structure and physical properties of materials[20, 21]. It has emerged as an effective strategy for controlling ferroelectric properties in both traditional perovskite-based films[22] and other 2D materials[19, 23]. Moreover, the strain gradient is inversely proportional to its relaxation length. The magnitude of the strain gradient and its corresponding induced effects in 2D materials are significantly amplified when strain is applied at the nanometer scale. For example, a strain gradient of 10^6 m^{-1} can be achieved by transferring MoS_2 onto a substrate with a microbeam[24, 25]. This can result in significant photovoltaic effect in centrosymmetric transferred flakes. Additionally, strain gradients can alter polarization[26, 27], control domain structures[28-30], modify hysteresis curves of ferroelectric thin films[31], and even induce large electric polarization in paraelectric crystals through the flexoelectric effect[23, 32, 33].

Molybdenum disulfide (MoS_2) is a prominent two-dimensional semiconductor material, renowned for its exceptional semiconductor properties, which have facilitated its extensive use in electronic and optoelectronic devices.[34, 35]. Previous studies have made significant strides in

exploring the phenomenon of sliding ferroelectricity within twisted 3R MoS_2 bilayers, uncovering a range of intriguing properties and potential applications. However, this area of research presents several challenges. A notable obstacle is the labour-intensive process required to fabricate twisted bilayers, further complicated by the typically small sizes of the resulting exfoliated samples. These limitations can restrict the scope of experimental research and hinder the practical application of potential devices. In response to these challenges, our research pivots towards exploring CVD-grown 2H MoS_2 samples, with a particular focus on the effects of strain on these samples. The application of 2H MoS_2 in nanoscale piezoelectrics has been hindered by its limited in-plane piezoelectric response, which is further characterized by an odd-even layer-number dependence. However, we propose a straightforward strategy that successfully induces a robust out-of-plane polarization in both strained monolayer MoS_2 (1L-MoS_2) and bilayer 2H MoS_2 (2L-MoS_2) samples. Remarkably, this approach also facilitates the generation of ferroelectric polarization in 2L-MoS_2 by employing a nanocone-patterned substrate. The piezoelectric coefficient (d_{33}) for strained 1L-MoS_2 was measured to be approximately 37.54 $pm \cdot V^{-1}$, while for 2L-MoS_2 it was around 24.80 $pm \cdot V^{-1}$. Furthermore, we successfully achieved polarization reversal in strained 2L-MoS_2 using Dual AC resonance (DART)-based piezoresponse force microscopy (PFM) technology. First-principles calculations revealed that the origin of sliding ferroelectricity in strained 2L-MoS_2 can be attributed to the lattice distortion and reconstruction of the 2L-MoS_2 induced by the nanocone substrate. Building upon these findings, we fabricated a ferroelectric tunnel junction (FTJ) and demonstrated that the reversibility of the ferroelectric polarization in the device can modify the tunnelling current density. This work establishes a

promising strategy for designing new 2D ferroelectric materials by strain engineering and expanding the family of 2D layered ferroelectric semiconductors.

2. RESULTS AND DISCUSSION

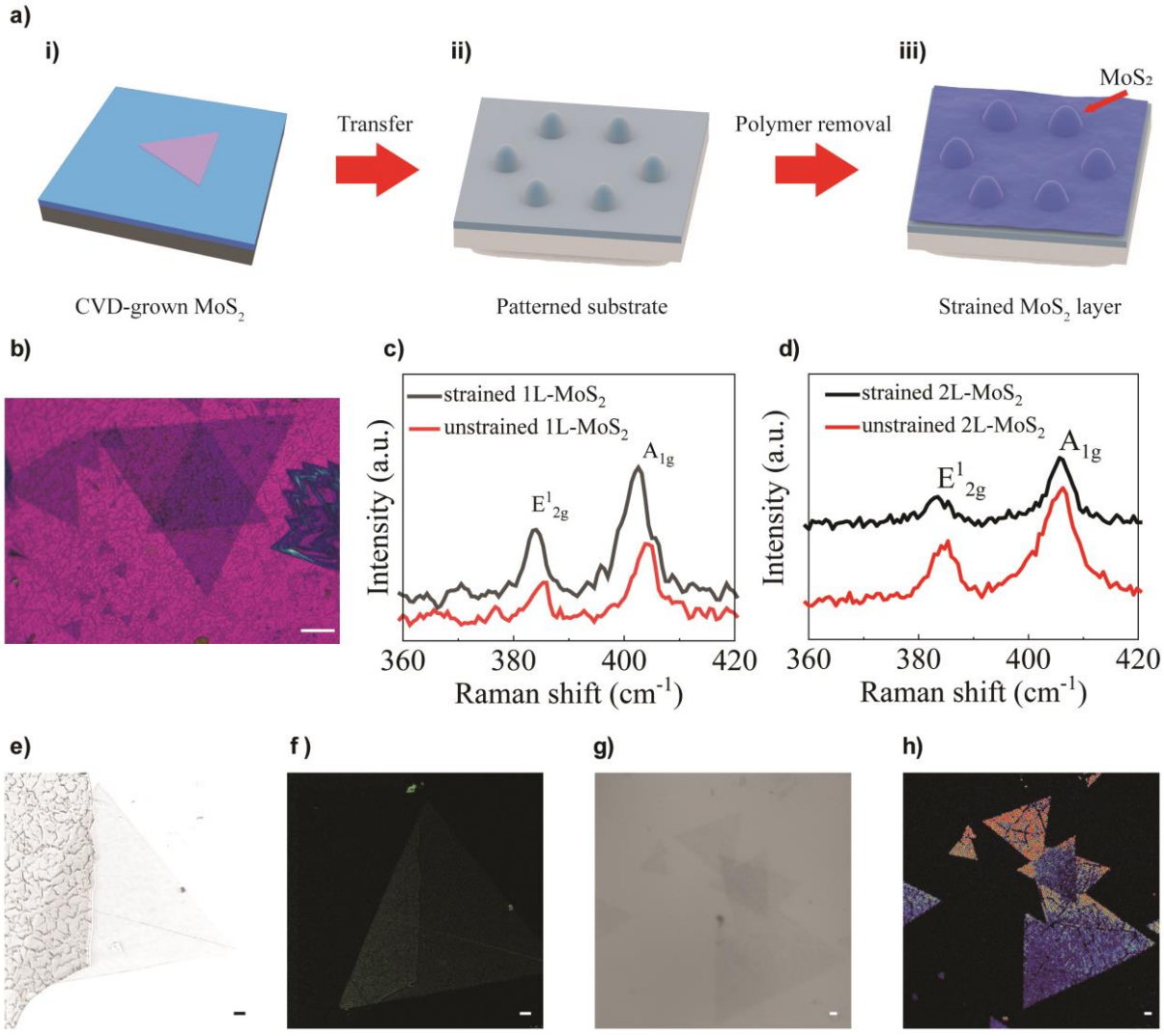

Figure 1. Characterizations of transferred CVD-grown MoS_2 samples on the patterned nanocone substrate. (a) Schematic illustration of the fabrication process for a strained MoS_2 layer on the patterned substrate. (b) Optical microscope image of the 2L-MoS_2 on the patterned substrate. The scale bar is 20 µm. Comparison of Raman spectra for (c) 1L-MoS_2 and (d) 2L-MoS_2 samples

transferred on the nanocone and flat substrate. (e) The optical microscopy image and (f) the corresponding SHG intensity map of the transferred 1L-MoS_2, with half of the sample on the flat substrate and half on the nanocone substrate. (g) The optical microscope image and (h) the corresponding SHG intensity map of the transferred 2L-MoS_2 sample. The scale bars are 5μm.

Detailed construction processes of strained MoS_2 sample are schematically illustrated in Figure 1a. In brief, MoS_2 sample was transferred on to the nanocone patterned substrate using the EVA-assisted method (see details in the Methods). The optical microscope image in Figure 1b illustrates the exceptional continuity of the MoS_2 samples on the fully patterned substrate with no discernible cracks or tears. A comprehensive Raman analysis was conducted to investigate the strain differences for 1L-MoS_2 and 2L-MoS_2 samples on the nanocone and on the flat SiO_2 surface. The results are depicted in Figures 1c and 1d. The unstrained 1L-MoS_2 sample demonstrates two pronounced modes: E^1_{2g} (~384.2 cm^{-1}) and A_{1g} (~403.1 cm^{-1}). The frequency difference between E^1_{2g} and A_{1g} is 18.9 cm^{-1}, a typical characteristic of 1L-MoS_2. By examining the redshift magnitudes of the Raman E^1_{2g} and A_{1g} peaks (2.46 cm^{-1} and 1.09 cm^{-1}, respectively), the average tensile strain in the 1L-MoS_2 sample was estimated to be 0.47%[36]. Besides, the unstrained 2L-MoS_2 sample displayed two prominent peaks at 383.49 cm^{-1} (E^1_{2g}) and 405.64 cm^{-1} (A_{1g}), with a frequency difference of 22.15 cm^{-1}. When subject to strain, the 2L-MoS_2 also exhibits significant redshifts in both E^1_{2g} and A_{1g} peaks (1.23 cm^{-1} and 0.62 cm^{-1}, respectively), correlating with a strain of 0.3% in the 2L-MoS_2 sample[36]. Figure 1e shows an optical microscopy image of transferred 1L-MoS_2 sample positioned across the boundary between the nanocone and flat substrate region. The left side corresponds to the nanocone substrate, while the right side is a flat substrate. Figure 1f

reveals that both the flat and nanocone regions of the 1L-MoS_2 displayed second harmonic generation (SHG) signal, which is in line with the asymmetric structure of MoS_2. Notably, the SHG response is significantly enhanced in the nanocone region compared to the flat region which can also be observed in previous studies[37]. This enhancement is probably due to the crystal lattice deformation in the 1L-MoS_2 sample. To examine the broken inversion symmetry in the strained 2L-MoS_2, we conducted additional SHG measurement (Figure 1g). As shown in Figure 1h, the SHG response from the 2L-MoS_2 sample on the nanocone substrate is clearly visible, while no SHG signal can be observed from the 2L-MoS_2 sample on a flat substrate (see Figure S1). This implies that the strain induced by the patterned nanocone can break the symmetric structure of 2L-MoS_2. Moreover, the SHG intensity of the 2L-MoS_2 sample is lower than that of the 1L-MoS_2 sample, which is in agreement with the Raman analysis indicating a reduced tendency for strain via the nanocone substrate as the layer thickness of MoS_2 increases.

DART-based PFM technology was utilized to investigate the out-of-plane polarization of strained MoS_2 samples transferred on the nanocone substrate. The AFM topography of the triangular 1L-MoS_2 sample covering on the nanocone substrate is shown in Figure 2a, manifesting that the transferred sample is continuous and undamaged. To determine the effective out-of-plane piezoelectric coefficient, tip voltages from 2.5 V to 3.5 V were applied to study the vertical electromechanical responses of the MoS_2 samples. The amplitude images under different tip voltages are shown in Figures 2b-d. Inspiringly, significant amplitude changes were observed when different tip voltages were applied, indicating strong inverse piezoelectric effect. The piezoresponse amplitudes in Figure 2j are obtained from the average amplitude variations between the 1L-MoS_2 sample and the substrate. Through the analysis of average amplitude

variations concerning applied voltages, the 1L-MoS_2 sample exhibits a remarkably high d_{33}^{eff} value of approximately 18.77 pm·V^{-1}. According to previous reports, the actual piezoelectric coefficient (d_{33}) is roughly twice the measured d_{33}^{eff}. Based on this, we can estimate the d_{33} value to be approximately 37.54 pm·V^{-1} for strained 1L-MoS_2 and about 24.80 pm·V^{-1} for 2L-MoS_2, surpassing that of most reported piezoelectric materials as summarized in Table S1. Two potential origins could contribute to this exceptional d_{33} coefficient. First, the tight contact between the 1L-MoS_2 sample and nanocones generates an out-of-plane polarization component resulting from the intrinsic in-plane polarization in the 1L-MoS_2. Second, the strained 1L-MoS_2 induces a substantial strain gradient of over 10^6 m^{-1} on the patterned substrate, which gives rise to a noticeable out-of-plane flexoelectric polarization[38, 39]. The latter shall be the predominant factor contributing to the detected vertical polarization, given that the in-plane piezoelectric coefficient (d_{11}) of the MoS_2 monolayer is merely 3.06 pm·V^{-1} [40]. In comparison, a much smaller d_{33} coefficient with the value of 3.08 pm V^{-1} was measured at flat MoS_2 regions (Figure S2)[41]. The weak electromechanical response from the flat 1L-MoS_2 sample can be attributed to the tip and surface electrostatic interaction since neither out-of-plane piezoelectricity nor flexoelectricity is induced.

To gain further insights into the vertical electromechanical coupling of MoS_2 flakes, we also conducted comprehensive PFM measurements on 2L-MoS_2 samples. The 2L-MoS_2 sample, shown in Figure 2e, was fabricated by transferring one chemical vapor deposition (CVD)-grown MoS_2 monolayer onto another with antiparallel orientation. Subsequently, the entire 2L-MoS_2 sample was transferred onto a nanocone substrate using the EVA-assisted method. It is worth noting that the 2L-MoS_2 flake intrinsically possesses a centrosymmetric structure, implying the absence

of in-plane and out-of-plane piezoelectricity. Interestingly, despite its centrosymmetric nature, we observed obvious out-of-plane polarization in the 2L-MoS_2 sample once it was transferred onto the nanocone substrate. Figures 2f-i show the PFM amplitude images with increasing drive voltages, ranging from 2 V to 3.5 V in increments of 0.5 V. The vertical amplitude responses at the 1L-MoS_2 region are higher compared to that at the 2L-MoS_2 region, as indicated by the white lines. The observed vertical piezoelectric responses in both the strained 1L-MoS_2 and 2L-MoS_2 samples on the nanocone substrate highlight the presence of flexoelectricity, which differs from intrinsic piezoelectricity and is not confined by the number of layers[25, 42]. As is displayed from Figure 2k, the piezoelectric amplitudes of the MoS_2 samples are plotted as a function of AC driving voltages. The curve fitting analysis yielded a linear correlation, enabling the acquisition of d_{33} coefficients at ~36.9 pm V^{-1} for strained 1L-MoS_2 and ~24.80 pm V^{-1} for strained 2L-MoS_2 and illustrating a descending trend in the d_{33} coefficients with the increasing number of MoS_2 layers. This observation aligned with our SHG intensity analysis and is consistent with the findings from previous studies[19]. In order to exclude the potential influence of inhomogeneous electric fields between the PFM tip and samples on the observed vertical piezoelectricity in the 2L-MoS_2 sample, a comparative PFM measurement was carried out on 2L-MoS_2 samples transferred onto a flat substrate. The results revealed consistent noise levels across different drive voltages, denoting the absence of a piezoelectric signal in the unstrained 2L-MoS_2 sample. (Figure S2).

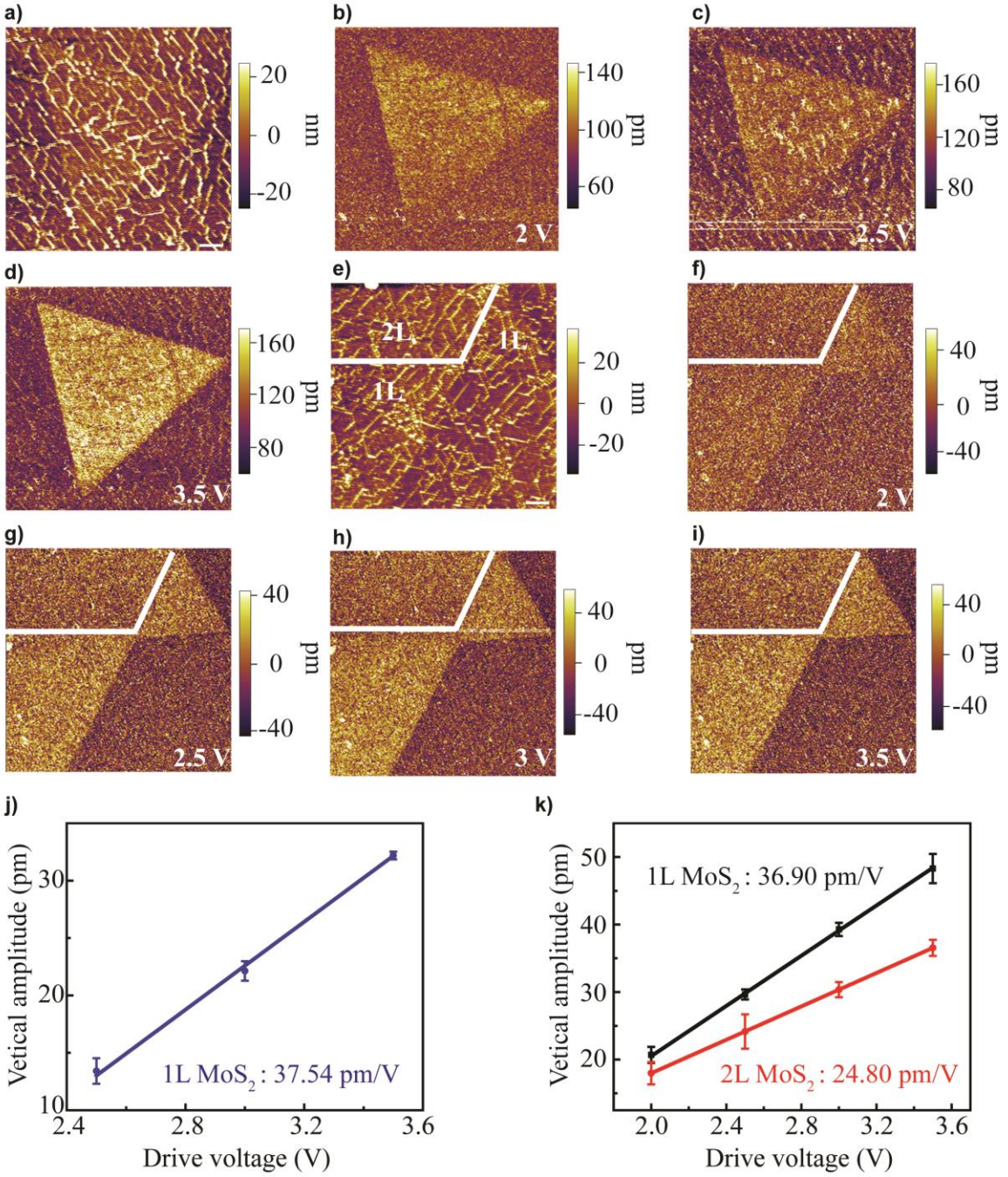

Figure 2. Existence of vertical piezoelectricity in the strained MoS_2. (a) The AFM topography of 1L-MoS_2. (b)-(d) The gradient of the amplitude images, observed by PFM with the applied tip voltages from 2.5 V to 3.5 V, reveals the remarkable vertical piezoelectricity of the 1L-MoS_2. (e)

Average piezoresponse amplitude of strained 1L-MoS_2 sample as a function of the applied AC voltage. (e) The AFM topography of the transferred MoS_2 sample. (f)-(i) Evolution of out-of-plane piezoresponses in the strained 1L-MoS_2 and 2L-MoS_2 samples transferred on the nanocone substrate concerning different drive voltages. (j)-(k) Average amplitude variations versus applied voltages. The scale bars are 5 µm.

The recent discovery of strain-induced ferroelectricity in 2D materials has sparked interest in the development of new 2D ferroelectric materials that hold promise for various electronic devices[19, 23]. This discovery serves as strong motivation for us to explore the presence of ferroelectricity in the strained MoS_2 samples. To verify the existence of ferroelectric behavior, it is crucial to demonstrate the ability to switch the material's polarization through an external electric field. Therefore, we investigated the local ferroelectric switchable behaviors in strained 2L-MoS_2 samples through PFM technique. Figures 3a and 3b illustrate the topography and height profile of the strained 2L-MoS_2 sample with the underlying nanocones of ~60 nm in height. Figures 3c and 3d present the PFM off-field hysteresis loops of the strained 2L-MoS_2 sample at different positions of the nanocone, as indicated by the red crosses in the height analysis. The amplitude loops exhibit a characteristic butterfly shape, while the phase loops displayed 180° phase difference between the two polarization states, providing evidence of ferroelectricity in the sample. Moreover, the two minima of the amplitude loop are consistent with the switching voltages observed in the phase signal, further confirming the presence of ferroelectric nature in the strained sample. It is noteworthy that the PFM off-field amplitude and phase responses of the strained 2L-MoS_2 sample displayed neglectable variations across different positions of the

nanocone. This observation suggests that, following the application of a threshold strain to induce ferroelectric behavior, additional strain does not significantly influence the appearance of polarization switching behavior in strained 2L-MoS_2.Similar findings have also been reported previously[23]. To ensure that the observed ferroelectric-like hysteresis loops are not resulting from the charging effects or ion migrations, we further conducted PFM hysteresis loops at different AC bias (V_{AC}) and measuring frequencies (Figure S3)[43]. The results show that the coercive voltage remained consistent regardless of the V_{AC} amplitudes and scanning frequencies, confirming the emerging ferroelectricity in the strained 2L-MoS_2. Particularly, there was no visible phase contrast in the strained 1L-MoS_2 and unstrained 2L-MoS_2 samples, indicating the absence of ferroelectricity without strain engineering (Figure S4). To provide further evidence of the ferroelectricity in strained 2L-MoS_2, we modify the ferroelectric polarization direction by writing two square patterns with opposite tip voltages ($\pm$10 V). The surface morphology, PFM amplitude and phase images after modification are displayed Figures 3e, 3f, and 3g, respectively. The clear PFM phase contrast in Figure 3g demonstrates the switchable antiparallel polarizations, signifying the successful bias modulation of polarization states and supporting the existence of out-of-plane ferroelectricity in strained 2L-MoS_2. In addition, similar PFM hysteresis loops can also be obtained in 2L-MoS_2 sample mechanically exfoliated from MoS_2 bulk crystal (Figures S5 and S6) on identical nanocone substrate. This finding further strengthens the presence of robust ferroelectric behaviors in strained 2L-MoS_2, independent of any possible defects introduced during the CVD growth process of the MoS_2 samples.

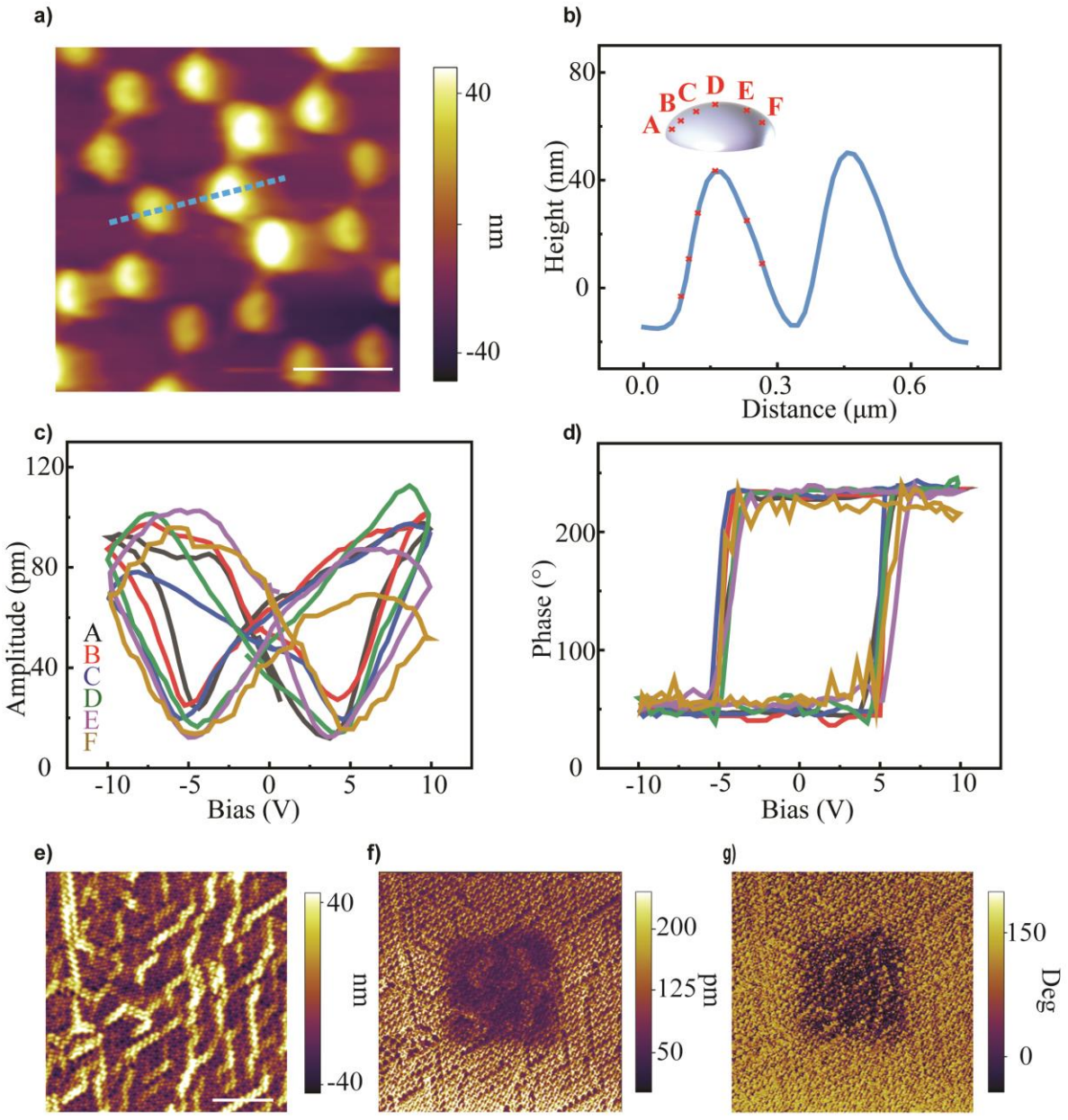

Figure 3. Ferroelectric switching of a 2L-MoS_2 sample transferred onto the conductive nanocone substrate. (a) AFM topography of the 2L-MoS_2 sample on the nanocone and (b) the corresponding height analysis of the nanocone across the blue dashed line with the red marked intersections indicating the positions for subsequent PFM amplitude and phase testing. The inset

showing a detailed schematic of the nanocone, highlighting the exact locations where PFM measurements are to be taken. The scale bar is 400 nm. (c) PFM amplitude and (d) phase hysteresis loops for 2L-MoS_2 with the DC field off at various nanocone positions. (e) AFM topography and the corresponding PFM (f) amplitude and (g) phase images of 2L-MoS_2 with ±10 V writing voltage in ambient conditions. The scale bars are 5 µm.

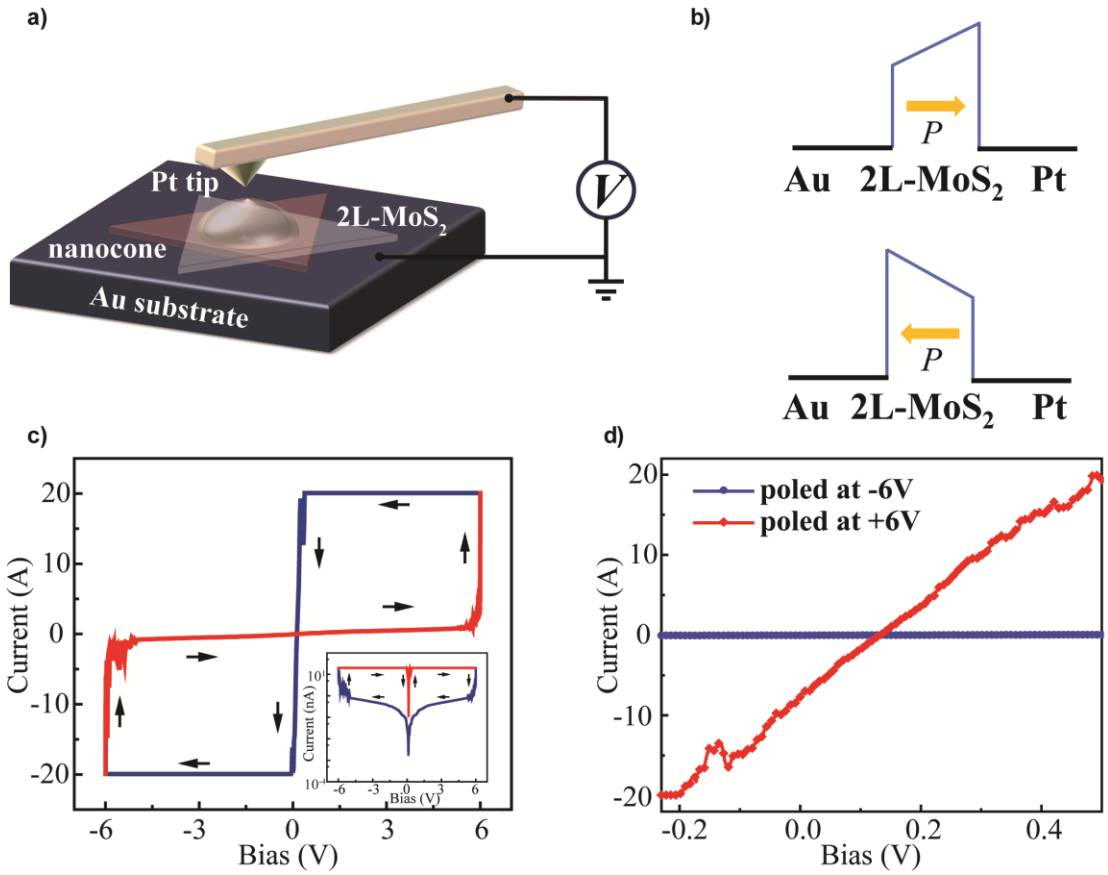

Figure 4. Polarization-dependent tunneling current versus applied bias in an FTJ device based on strained 2L-MoS_2. (a) A schematic illustration showing the conductive atomic force microscopy (C-AFM) set-up, where a conductive Pt tip is scanned on the 2L-MoS_2 transferred on the Au nanocone substrate. (b) Schematic illustration of the band diagram for the strained 2L-MoS_2-based FTJ device. (c) *I-V* characteristics of the strained 2L-MoS_2 FTJ device showing typical ferroelectric resistive switching behaviors. The inset showing the logarithmic *I-V* curve. (d) *I-V* characteristics of the FTJ device poled with different voltages.

To demonstrate the potential application of the ferroelectric strained 2L-MoS_2 flakes, we examined the transport properties of the fabricated samples in the vertical direction by conducting C-AFM measurements, and the corresponding experimental setup is shown in Figure 4a. Figure 4b displays the potential energy profiles for the ON and OFF states of the tunnelling junction, indicating that the resistance in the junction is strongly dependent on the ferroelectric polarization direction of the strained 2L-MoS_2 tunnel barrier. Typical *I-V* curve of the device was obtained within the voltage range of ±6 V, as illustrated in Figure 4c, with arrows indicating the voltage sweep directions. Sweeping the voltage from -6 to +6 V causes the ferroelectric tunnel junction (FTJ) device to transit from the OFF state to the ON state. Conversely, sweeping the voltage from +6 to -6 V switches the FTJ device back to the OFF state. This behavior arises from the effect in which a positive (negative) voltage higher than the coercive voltage (~5V) would induce a downward (upward) switching in the ferroelectric polarization, leading to electron accumulation (depletion) at the Pt interface and resulting in a decrease (increase) in the Schottky barrier. Figure 4d illustrates the *I-V* curves within the low-voltage range for the FTJ device in the

ON and OFF states. Negative poling with -6 V causes a reduction in the electron tunnelling current, placing the device in a high resistance state (HRS). Similarly, positive poling by +6 V switches the device to a low-resistance state (LRS). The ratio of tunnelling resistance between the two states is approximately 10^2, which might be limited by the current compliance of the C-AFM equipment set at 20 nA. The coercive voltage (~5 V) acquired from the *I-V* characteristics of the FTJ device well aligns with the value obtained from the local PFM off-field hysteresis measurements presented in Figure 3. The reliability of the device was confirmed through retention tests and *I-V* characteristics measured after 10 consecutive voltage sweep cycles, as shown in Fig. S7. The device was switched between low resistance state (LRS) and high resistance state (HRS) using a DC voltage sweep. And the retention performance of the device was obtained under the read voltage of 0.5 V. The resistance states of the FTJ device were maintained for 4000 s without external stimuli, demonstrating that the memory is non-volatile and stable. Consequently, strained 2L-MoS_2 exhibits ferroelectric properties, showing great potential for applications in memristor devices and ferroelectric transistors. Similar *I-V* characteristics was also observed in the exfoliated 2L-MoS_2 sample strained via the nanocone (Figure S8).

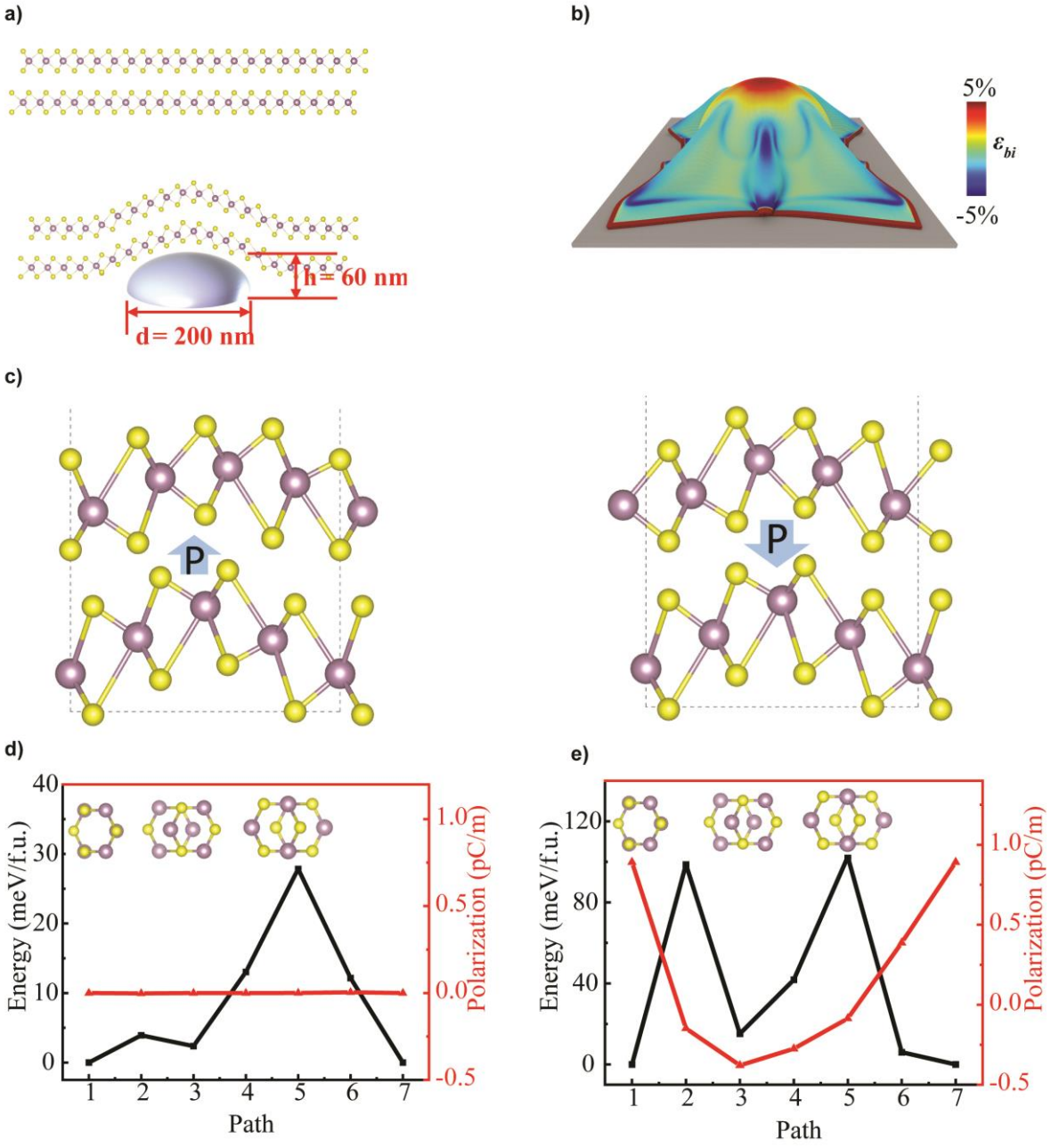

Figure 5. Theoretical analysis of out-of-plane ferroelectricity in the strained 2L-MoS_2. (a) Schematic illustrations of the 2L-MoS_2 on flat and nanocone substrates. (b) Strain map variation of the model shown in a. (c) Schematic model of out-of-plane switching coupling in the strained 2L-MoS_2. Relative energy and polarization of the 2L-MoS_2 stackings without (d) and with (e) strain as a function of sliding the top layer with respect to the bottom layer along the armchair direction

in the unit cell. The configurations AA (path 1), AB (path 3), BA (path 5) are marked and sketched above the plots.

For further and in-depth investigation of the origin of ferroelectric polarization in strained 2L-MoS_2, we conducted theoretical calculations to simulate the strain mapping, atomic structures and polarization behaviors. Figure 5a shows the side-view atomic structure of 2L-MoS_2 with AB stacking transferred onto flat and nanocone substrates, respectively. Figure 5b presents the strain distribution in 2L-MoS_2 conforming to a nanocone in which the geometry was determined from the experimental AFM data. The most strained regions of the 2L-MoS_2 exhibit local strains up to 5%, corresponds a strain gradient of around 10^7 m^{-1}. Such significant gradient induces local inversion symmetry breaking in an otherwise centrosymmetric material. It is important to point out that the strain levels indicated by our simulations are substantially higher than those inferred from Raman spectroscopy, which provides an averaged strain value due to the finite size of the laser spot used in optical measurements. Our computational models, which incorporate accurate values for the elastic deformation potential of MoS_2 (Figure 5c), demonstrate that the large strain induced by the nanocone promotes lattice distortion and reconstruction in 2L-MoS_2, potentially giving rise to moiré patterns. This phenomenon was also observed by other studies[44]. As shown in Figure 5d, the flat 2L-MoS_2 exhibits a centrosymmetric structure across all stacking configurations, resulting in zero polarization. On the contrary, when transferred onto the nanocone substrate (Figure 5e), the strained 2L-MoS_2 displays a minor, yet non-zero local dipole density across various stacking configurations. Our findings reveal that the atomic structures of two different stacking configurations of 2L-MoS_2 (AA-P_{up} and AB-P_{down}) are differentiated by a

lateral slide along the armchair direction. While the AA-P_{up} configuration exhibits an out-of-plane polarization of 0.89 pC m^{-1}, the AB-P_{down} configuration presents a negative value of -0.38 pC m^{-1}. As a result, the vertical polarization in the strained 2L-MoS_2 could be reversed through a lateral slide between the two monolayers that overcomes a sliding barrier of 98 meV/f.u, indicating ferroelectric behavior.

3. CONCLUSIONS

In conclusion, this study presents a comprehensive analysis of the vertical polarization induced by the nanocone-patterned substrate in both 1L-MoS_2 and 2L-MoS_2. A significant finding of our study is the unexpected emergence of vertical ferroelectricity in strained 2L-MoS_2. The existence of out-of-plane ferroelectricity was consistently observed regardless of preparation method of the 2L-MoS_2, thereby attesting to the versatility and reproducibility of our strain engineering approach. The d_{33} coefficients were carefully observed and quantified, with remarkably high values of for strined1L-MoS_2 and 2L-MoS_2, respectively. These extraordinary outcomes can be attributed to the strain gradient induced via the nanocone. Furthermore, we conducted an in-depth investigation into the strain engineering of the ferroelectric transition in the centrosymmetric 2H MoS_2 semiconductor, utilizing both the PFM technique and first-principles calculations. The sliding of MoS_2 layers between each other and distortion of MoS_2 lattice were found to be a critical factor for the emergence of ferroelectricity in the strained 2L-MoS_2. For demonstration, a prototype of ferroelectric nanodevices has been proposed, leveraging vertical polarization in strained 2L-MoS_2, illustrating the potential for applications in non-volatile and advanced electronics.

4. METHODS

Growth of MoS_2. CVD method was used to grow 2H-MoS_2 samples in a tube furnace. A mixed powder of MoO_3 and NaCl (2:1) was placed in a quartz tube, and a Si/SiO_2 wafer was used as the growth substrate, which was suspended in the tube. Before each growth, oxygen was removed by purging with Ar and pumping. The growth was conducted at 750 °C with 30 sccm Ar flow at atmospheric pressure for 8 min.

Sample fabrication. The standard polymer stamp dry-transfer technique was used to prepare 2L-MoS_2 samples on a modified optical microscope with a heating stage and a rotation stage. The MoS_2 monolayer was brought into contact with a glass slide with a polyvinyl alcohol (PVA) film. The 2L-MoS_2 sample was prepared by stacking 1L-MoS_2 in an antiparallel orientation. EVA solution (Aldrich, vinyl acetate 40 wt %, 10 wt % dissolved in xylene) was used to transfer stacked 2L-MoS_2 and as-grown 1L-MoS_2 samples onto a gold nanocone substrate (see SI Note for more details). The transferred sample was then baked at 80 °C for 2 hours and soaked in xylene for 30 min to remove the EVA film.

Characterization methods. Raman measurements were carried out using a WITEC alpha 500 Confocal Raman system equipped with the 532-nm laser source. The Raman spectra was collected by an Olympus 100 × objective (N.A. = 0.9) and dispersed by 1,800 with excitation laser power lower than 1 mW. A Ti:sapphire femtosecond laser with the wavelength of 900 nm was used to examine SHG signals of samples. PFM measurements were carried out on a commercial atomic force microscope (Asylum Research MFP-3D), where the Pt/Ir-coated Si cantilever tips were driven with an ac voltage under the tip-sample contact resonant frequency (~300 kHz). PFM images and hysteresis loops were collected in the DART PFM mode. The electrical transport

characteristics of the devices were characterized by measuring the I-V curves of the devices using C-AFM at room temperature.

DFT simulations. All the first-principles calculations are performed by using density functional theory (DFT) implemented in the Vienna ab initio simulation package (version 6.1.1). The Perdew-Burke-Ernzerhof exchange-correlation functional form of the generalized gradient approximation and the projector augmented wave potentials are adopted for the interaction between the valence electrons and cores. The plane-wave expansion cutoff energy is set to 450 eV, and the Γ-centered Brillouin zone is sampled with 3 × 10 × 1 k-points mesh using the Monkhorst-pack scheme. In this study, we have considered six idealized model structures based on bilayer 2H MoS_2, in which the top layers of 2H MoS_2 structures are slidden along the a-axis step by step, with the aspect ratio of ripples are set as the same as the experiment. The DFT-D3 functional of Grimme is used as vdW correction.

Modelling of strain distribution of MoS_2 on nanocones. In this study, molecular dynamics (MD) simulations was employed to investigate the geometric morphology of double-layered MoS_2 sheets conforming to a gold nanocone-based nanostructure. The MoS_2 sheets are modelled as a hexagonal honeycomb lattice with dimensions of approximately 3991.12 × 4110.84 $Å^2$. The underlying gold substrate is represented by a face-centred cubic (FCC) lattice with a lattice constant of 4.0783 Å and features a nanocone structure on a flat gold plane, measuring 4013.52 × 4130.56 $Å^2$. The combined structure of the gold semi-sphere and cone has a diameter of 2000 Å. To eliminate potential surface effects, we apply periodic boundary conditions (PBCs) along the planar directions of the MoS_2 sheets, while a wall-boundary condition is used in the perpendicular direction to prevent interactions with periodic images of the sheets. The atomic interactions

within the system are described using a many-body reactive empirical bond order (REBO)-type potential for Mo-S interactions[45], and a many-body embedded-atom method (EAM) potential for the gold substrate[46]. For the non-bonded van der Waals' interactions between MoS_2 sheets and gold substrate, the 12-6 Lennard-Jones (LJ) potential with cutoff distance of 10.0 Å is applied, in which the LJ parameters are taken from universal forcefield (UFF) based on the Lorentz-Berthelot mixing rules[47]. Before commencing the MD simulations, we first perform energy minimization to relax the double-layered 2H MoS_2 sheets. Subsequently, MD simulations are conducted for 400,000 timesteps within the NVT ensemble (constant number of particles, volume, and temperature) to assess the strain distribution in the 2H MoS_2 sheets. During these simulations, a constant force is applied to each atom of the MoS_2 sheets in a downward direction to ensure proper coverage over the nanocone. It is important to note that the gold substrate remains stationary throughout the simulation process. The motion of atoms in the system is governed by classical Newtonian mechanics, which are resolved using the velocity-Verlet integration algorithm with a timestep of 1.0 fs. All MD simulations are performed using the Large-scale Atomic/Molecular Massively Parallel Simulator (LAMMPS) software package.

ASSOCIATED CONTENT

AUTHOR INFORMATION

Corresponding Author

* Jianhua Hao - Department of Applied Physics, The Hong Kong Polytechnic University, Hung Hom, Hong Kong 999077, P. R. China; The Hong Kong Polytechnic University Shenzhen Research

Institute, Shenzhen 518057, P. R. China; Research Centre for Nanoscience and Nanotechnology, The Hong Kong Polytechnic University, Hong Kong 999077, China

Email: jh.hao@polyu.edu.hk

Authors

Jianfeng Mao - Department of Applied Physics, The Hong Kong Polytechnic University, Hung Hom, Hong Kong 999077, P. R. China; The Hong Kong Polytechnic University Shenzhen Research Institute, Shenzhen 518057, P. R. China

Jingyu He - Department of Applied Physics, The Hong Kong Polytechnic University, Hung Hom, Hong Kong 999077, P. R. China

Weng Fu Io - Department of Applied Physics, The Hong Kong Polytechnic University, Hung Hom, Hong Kong 999077, P. R. China

Feng Guo - Department of Applied Physics, The Hong Kong Polytechnic University, Hung Hom, Hong Kong 999077, P. R. China; The Hong Kong Polytechnic University Shenzhen Research Institute, Shenzhen 518057, P. R. China

Zehan Wu - Department of Applied Physics, The Hong Kong Polytechnic University, Hung Hom, Hong Kong 999077, P. R. China; The Hong Kong Polytechnic University Shenzhen Research Institute, Shenzhen 518057, P. R. China

Ming Yang - Department of Applied Physics, The Hong Kong Polytechnic University, Hung Hom, Hong Kong 999077, P. R. China; Research Centre for Nanoscience and Nanotechnology, The Hong Kong Polytechnic University, Hong Kong 999077, P. R. China

Notes

The authors declare no competing financial interest.

ACKNOWLEDGMENT

This work was supported by the grants from Research Grants Council of Hong Kong (SRFS 2122-5S02), National Natural Science Foundation of China (No. 52233014), and PolyU Grants (1-CE0H and 1-CD7V).

5. REFERENCE

(1) Si, M.; Saha, A. K.; Gao, S.; Qiu, G.; Qin, J.; Duan, Y.; Jian, J.; Niu, C.; Wang, H.; Wu, W. A ferroelectric semiconductor field-effect transistor. *Nat. Electron.* **2019**, *2* (12), 580-586. DOI: 10.1038/s41928-019-0338-7.

(2) Xue, F.; He, X.; Wang, Z.; Retamal, J. R. D.; Chai, Z.; Jing, L.; Zhang, C.; Fang, H.; Chai, Y.; Jiang, T. Giant ferroelectric resistance switching controlled by a modulatory terminal for low-power neuromorphic in-memory computing. *Adv. Mater.* **2021**, *33* (21), 2008709. DOI: 10.1002/adma.202008709.

(3) Martin, L. W.; Rappe, A. M. Thin-film ferroelectric materials and their applications. *Nat. Rev. Mater.* **2016**, *2* (2), 1-14. DOI: 10.1038/natrevmats.2016.87.

(4) Mikolajick, T.; Slesazeck, S.; Mulaosmanovic, H.; Park, M.; Fichtner, S.; Lomenzo, P.; Hoffmann, M.; Schroeder, U. Next generation ferroelectric materials for semiconductor process integration and their applications. *J. Appl. Phys.* **2021**, *129* (10). DOI: 10.1063/5.0037617.

(5) Libanori, A.; Chen, G.; Zhao, X.; Zhou, Y.; Chen, J. Smart textiles for personalized healthcare. *Nat. Electron.* **2022**, *5* (3), 142-156. DOI: 10.1038/s41928-022-00723-z.

(6) Chen, G.; Xiao, X.; Zhao, X.; Tat, T.; Bick, M.; Chen, J. Electronic textiles for wearable point-of-care systems. *Chem. Rev.* **2021**, *122* (3), 3259-3291. DOI: 10.1021/acs.chemrev.1c00502.

(7) Chang, K.; Liu, J.; Lin, H.; Wang, N.; Zhao, K.; Zhang, A.; Jin, F.; Zhong, Y.; Hu, X.; Duan, W. Discovery of robust in-plane ferroelectricity in atomic-thick SnTe. *Science* **2016**, *353* (6296), 274-278. DOI: 10.1126/science.aad860.

(8) Liu, F.; You, L.; Seyler, K. L.; Li, X.; Yu, P.; Lin, J.; Wang, X.; Zhou, J.; Wang, H.; He, H. Room-temperature ferroelectricity in $CuInP_2S_6$ ultrathin flakes. *Nat. Commun.* **2016**, *7* (1), 1-6. DOI: 10.1038/ncomms12357

(9) Yuan, S.; Luo, X.; Chan, H. L.; Xiao, C.; Dai, Y.; Xie, M.; Hao, J. Room-temperature ferroelectricity in $MoTe_2$ down to the atomic monolayer limit. *Nat. Commun.* **2019**, *10* (1), 1775. DOI: 10.1038/s41467-019-09669-x.

(10) Io, W. F.; Yuan, S.; Pang, S. Y.; Wong, L. W.; Zhao, J.; Hao, J. Temperature-and thickness-dependence of robust out-of-plane ferroelectricity in CVD grown ultrathin van der Waals α-In_2Se_3 layers. *Nano Res.* **2020**, *13*, 1897-1902. DOI: 10.1007/s12274-020-2640-0.

(11) Io, W. F.; Pang, S.-Y.; Wong, L. W.; Zhao, Y.; Ding, R.; Mao, J.; Zhao, Y.; Guo, F.; Yuan, S.; Zhao, J. Direct observation of intrinsic room-temperature ferroelectricity in 2D layered $CuCrP_2S_6$. *Nat. Commun.* **2023**, *14* (1), 7304. DOI: 10.1038/s41467-023-43097-2.

(12) Li, L.; Wu, M. Binary compound bilayer and multilayer with vertical polarizations: two-dimensional ferroelectrics, multiferroics, and nanogenerators. *ACS Nano* **2017**, *11* (6), 6382-6388. DOI: 10.1021/acsnano.7b02756

(13) Yasuda, K.; Wang, X.; Watanabe, K.; Taniguchi, T.; Jarillo-Herrero, P. Stacking-engineered ferroelectricity in bilayer boron nitride. *Science* **2021**, *372* (6549), 1458-1462. DOI:

10.1126/science.abd3230

(14) Lv, M.; Sun, X.; Chen, Y.; Taniguchi, T.; Watanabe, K.; Wu, M.; Wang, J.; Xue, J. Spatially resolved polarization manipulation of ferroelectricity in twisted hBN. *Adv. Mater.* **2022**, *34* (51), e2203990. DOI: 10.1002/adma.202203990.

(15) Fei, Z.; Zhao, W.; Palomaki, T. A.; Sun, B.; Miller, M. K.; Zhao, Z.; Yan, J.; Xu, X.; Cobden, D. H. Ferroelectric switching of a two-dimensional metal. *Nature* **2018**, *560* (7718), 336-339. DOI: 10.1038/s41586-018-0336-3.

(16) Deb, S.; Cao, W.; Raab, N.; Watanabe, K.; Taniguchi, T.; Goldstein, M.; Kronik, L.; Urbakh, M.; Hod, O.; Ben Shalom, M. Cumulative polarization in conductive interfacial ferroelectrics. *Nature* **2022**. DOI: 10.1038/s41586-022-05341-5.

(17) Wang, X.; Yasuda, K.; Zhang, Y.; Liu, S.; Watanabe, K.; Taniguchi, T.; Hone, J.; Fu, L.; Jarillo-Herrero, P. Interfacial ferroelectricity in rhombohedral-stacked bilayer transition metal dichalcogenides. *Nat. Nanotechnol.* **2022**, *17* (4), 367-371. DOI: 10.1038/s41565-021-01059-z.

(18) Meng, P.; Wu, Y.; Bian, R.; Pan, E.; Dong, B.; Zhao, X.; Chen, J.; Wu, L.; Sun, Y.; Fu, Q.; et al. Sliding induced multiple polarization states in two-dimensional ferroelectrics. *Nat. Commun.* **2022**, *13* (1), 7696. DOI: 10.1038/s41467-022-35339-6.

(19) Sui, F.; Jin, M.; Zhang, Y.; Qi, R.; Wu, Y. N.; Huang, R.; Yue, F.; Chu, J. Sliding ferroelectricity in van der Waals layered γ-InSe semiconductor. *Nat. Commun.* **2023**, *14* (1), 36. DOI: 10.1038/s41467-022-35490-0.

(20) Kato, Y.; Myers, R.; Gossard, A.; Awschalom, D. Coherent spin manipulation without magnetic fields in strained semiconductors. *Nature* **2004**, *427* (6969), 50-53. DOI: 10.1038/nature02202.

(21) Yang, S.; Chen, Y.; Jiang, C. Strain engineering of two-dimensional materials: methods,

properties, and applications. *InfoMat* **2021**, *3* (4), 397-420. DOI: 10.1002/inf2.12177.

(22) Xu, R.; Huang, J.; Barnard, E. S.; Hong, S. S.; Singh, P.; Wong, E. K.; Jansen, T.; Harbola, V.; Xiao, J.; Wang, B. Y.; et al. Strain-induced room-temperature ferroelectricity in $SrTiO_3$ membranes. *Nat. Commun.* **2020**, *11* (1), 3141. DOI: 10.1038/s41467-020-16912-3.

(23) Wu, M.; Lou, Z.; Dai, C. M.; Wang, T.; Wang, J.; Zhu, Z.; Xu, Z.; Sun, T.; Li, W.; Zheng, X. Achieving Ferroelectricity in a Centrosymmetric High-Performance Semiconductor by Strain Engineering. Adv. Mater. **2023**, 2300450. DOI: 10.1002/adma.202300450.

(24) Maiti, R.; Patil, C.; Saadi, M. A. S. R.; Xie, T.; Azadani, J. G.; Uluutku, B.; Amin, R.; Briggs, A. F.; Miscuglio, M.; Van Thourhout, D.; et al. Strain-engineered high-responsivity $MoTe_2$ photodetector for silicon photonic integrated circuits. *Nat. Photonics* **2020**, *14* (9), 578-584. DOI: 10.1038/s41566-020-0647-4.

(25) Jiang, J.; Chen, Z.; Hu, Y.; Xiang, Y.; Zhang, L.; Wang, Y.; Wang, G. C.; Shi, J. Flexo-photovoltaic effect in MoS_2. *Nat. Nanotechnol.* **2021**. DOI: 10.1038/s41565-021-00919-y.

(26) Park, S. M.; Wang, B.; Paudel, T.; Park, S. Y.; Das, S.; Kim, J. R.; Ko, E. K.; Lee, H. G.; Park, N.; Tao, L.; et al. Colossal flexoresistance in dielectrics. *Nat. Commun.* **2020**, *11* (1), 2586. DOI: 10.1038/s41467-020-16207-7.

(27) Wang, L.; Liu, S.; Feng, X.; Zhang, C.; Zhu, L.; Zhai, J.; Qin, Y.; Wang, Z. L. Flexoelectronics of centrosymmetric semiconductors. *Nat. Nanotechnol.* **2020**, *15* (8), 661-667. DOI: 10.1038/s41565-020-0700-y.

(28) Lun, Y.; Wang, X.; Kang, J.; Ren, Q.; Wang, T.; Han, W.; Gao, Z.; Huang, H.; Chen, Y.; Chen, L. Q.; et al. Ultralow tip-force driven sizable-area domain manipulation through transverse flexoelectricity. *Adv. Mater.* **2023**, e2302320. DOI: 10.1002/adma.202302320.

(29) Ming, W.; Huang, B.; Zheng, S.; Bai, Y.; Wang, J.; Wang, J.; Li, J. Flexoelectric engineering of van der Waals ferroelectric $CuInP_2S_6$. *Sci. Adv.* **2022**, *8* (33), eabq1232. DOI: 10.1126/sciadv.abq1232.

(30) Lu, H.; Bark, C.-W.; Esque De Los Ojos, D.; Alcala, J.; Eom, C.-B.; Catalan, G.; Gruverman, A. Mechanical writing of ferroelectric polarization. *Science* **2012**, *336* (6077), 59-61. DOI: 10.1126/science.121869.

(31) Chen, C.; Liu, H.; Lai, Q.; Mao, X.; Fu, J.; Fu, Z.; Zeng, H. Large-Scale Domain Engineering in Two-dimensional ferroelectric $CuInP_2S_6$ via giant flexoelectric effect. *Nano Lett.* **2022**, *22* (8), 3275-3282. DOI: 10.1021/acs.nanolett.2c00130.

(32) Haeni, J.; Irvin, P.; Chang, W.; Uecker, R.; Reiche, P.; Li, Y.; Choudhury, S.; Tian, W.; Hawley, M.; Craigo, B. Room-temperature ferroelectricity in strained $SrTiO_3$. *Nature* **2004**, *430* (7001), 758-761. DOI: 10.1038/nature02773.

(33) Jang, H. W.; Kumar, A.; Denev, S.; Biegalski, M. D.; Maksymovych, P.; Bark, C. W.; Nelson, C. T.; Folkman, C. M.; Baek, S. H.; Balke, N.; et al. Ferroelectricity in strain-free $SrTiO_3$ thin films. *Phys Rev. Lett.* **2010**, *104* (19), 197601. DOI: 10.1103/PhysRevLett.104.197601.

(34) Bai, G.; Lyu, Y.; Wu, Z.; Xu, S.; Hao, J. Lanthanide near-infrared emission and energy transfer in layered WS_2/MoS_2 heterostructure. *Sci. China Mater.* **2020**, *63* (4), 575-581. DOI: 10.1007/s40843-019-1232-2.

(35) Manzeli, S.; Ovchinnikov, D.; Pasquier, D.; Yazyev, O. V.; Kis, A. 2D transition metal dichalcogenides. *Nat. Rev. Mater.* **2017**, *2* (8), 1-15. DOI: 10.1038/natrevmats.2017.33.

(36) Lloyd, D.; Liu, X.; Christopher, J. W.; Cantley, L.; Wadehra, A.; Kim, B. L.; Goldberg, B. B.; Swan, A. K.; Bunch, J. S. Band Gap Engineering with ultralarge biaxial strains in suspended monolayer

MoS_2. *Nano Lett.* **2016**, *16* (9), 5836-5841. DOI: 10.1021/acs.nanolett.6b02615.

(37) Li, D.; Wei, C.; Song, J.; Huang, X.; Wang, F.; Liu, K.; Xiong, W.; Hong, X.; Cui, B.; Feng, A.; et al. Anisotropic enhancement of second-harmonic generation in monolayer and bilayer MoS_2 by Integrating with TiO_2 nanowires. *Nano Lett.* **2019**, *19* (6), 4195-4204. DOI: 10.1021/acs.nanolett.9b01933.

(38) Li, H.; Contryman, A. W.; Qian, X.; Ardakani, S. M.; Gong, Y.; Wang, X.; Weisse, J. M.; Lee, C. H.; Zhao, J.; Ajayan, P. M.; et al. Optoelectronic crystal of artificial atoms in strain-textured molybdenum disulphide. *Nat. Commun.* **2015**, *6*, 7381. DOI: 10.1038/ncomms8381.

(39) Feng, J.; Qian, X.; Huang, C.-W.; Li, J. Strain-engineered artificial atom as a broad-spectrum solar energy funnel. *Nat. Photonics* **2012**, *6* (12), 866-872. DOI: 10.1038/nphoton.2012.285.

(40) Han, S. A.; Kim, T. H.; Kim, S. K.; Lee, K. H.; Park, H. J.; Lee, J. H.; Kim, S. W. Point-defect-passivated MoS_2 nanosheet-based high performance piezoelectric nanogenerator. *Adv. Mater.* **2018**, *30* (21), e1800342. DOI: 10.1002/adma.201800342.

(41) Brennan, C. J.; Ghosh, R.; Koul, K.; Banerjee, S. K.; Lu, N.; Yu, E. T. Out-of-plane electromechanical response of monolayer molybdenum disulfide measured by piezoresponse force microscopy. *Nano Lett.* **2017**, *17* (9), 5464-5471. DOI: 10.1021/acs.nanolett.7b02123.

(42) Sun, L.; Javvaji, B.; Zhang, C.; Zhuang, X.; Chen, W. Effect of flexoelectricity on a bilayer molybdenum disulfide Schottky contact. *Nano Energy* **2022**, *102*, 107701. DOI: 10.1016/j.nanoen.2022.107701.

(43) Rogée, L.; Wang, L.; Zhang, Y.; Cai, S.; Wang, P.; Chhowalla, M.; Ji, W.; Lau, S. P. Ferroelectricity in untwisted heterobilayers of transition metal dichalcogenides. *Science* **2022**, *376* (6596), 973-978. DOI: 10.1126/science.abm573.

(44) Pimenta Martins, L. G.; Ruiz-Tijerina, D. A.; Occhialini, C. A.; Park, J. H.; Song, Q.; Lu, A. Y.; Venezuela, P.; Cancado, L. G.; Mazzoni, M. S. C.; Matos, M. J. S.; et al. Pressure tuning of minibands in MoS_2/WSe_2 heterostructures revealed by moire phonons. *Nat. Nanotechnol.* **2023**, *18* (10), 1147-1153. DOI: 10.1038/s41565-023-01413-3.

(45) Yang, L.; Liu, J.; Lin, Y.; Xu, K.; Cao, X.; Zhang, Z.; Wu, J. Strengthening and weakening by dislocations in monolayer MoS_2. *Chem. Mater.* **2021**, *33* (22), 8758-8767. DOI: 10.1021/acs.chemmater.1c02797.

(46) Foiles, S.; Baskes, M.; Daw, M. S. Embedded-atom-method functions for the fcc metals Cu, Ag, Au, Ni, Pd, Pt, and their alloys. *Phys. Rev. B* **1986**, *33* (12), 7983. DOI: 10.1103/PhysRevB.33.7983.

(47) Rappé, A. K.; Casewit, C. J.; Colwell, K.; Goddard III, W. A.; Skiff, W. M. UFF, a full periodic table force field for molecular mechanics and molecular dynamics simulations. *J. Am. Chem. Soc.* **1992**, *114* (25), 10024-10035. DOI: 10.1021/ja00051a040.

TABLE OF CONTENTS

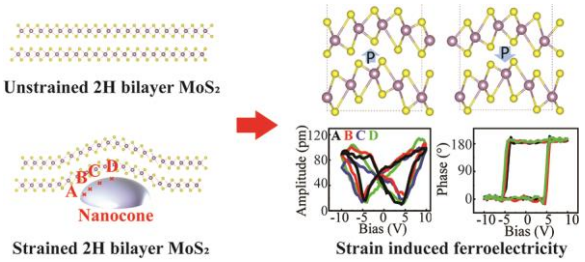

Supporting Information

Strain-engineered ferroelectricity in 2H bilayer MoS_2

Jianfeng Mao[1,2], Jingyu He[1], Weng Fu Io[1], Feng Guo[1,2], Zehan Wu[1,2], Ming Yang[1,3], Jianhua Hao[1,2,3]*

1 Department of Applied Physics, The Hong Kong Polytechnic University, Hung Hom, Hong Kong 999077, P. R. China

2 The Hong Kong Polytechnic University Shenzhen Research Institute, Shenzhen 518057, P. R. China

3 Research Centre for Nanoscience and Nanotechnology, The Hong Kong Polytechnic University, Hong Kong 999077, P. R. China

* Corresponding authors: jh.hao@polyu.edu.hk

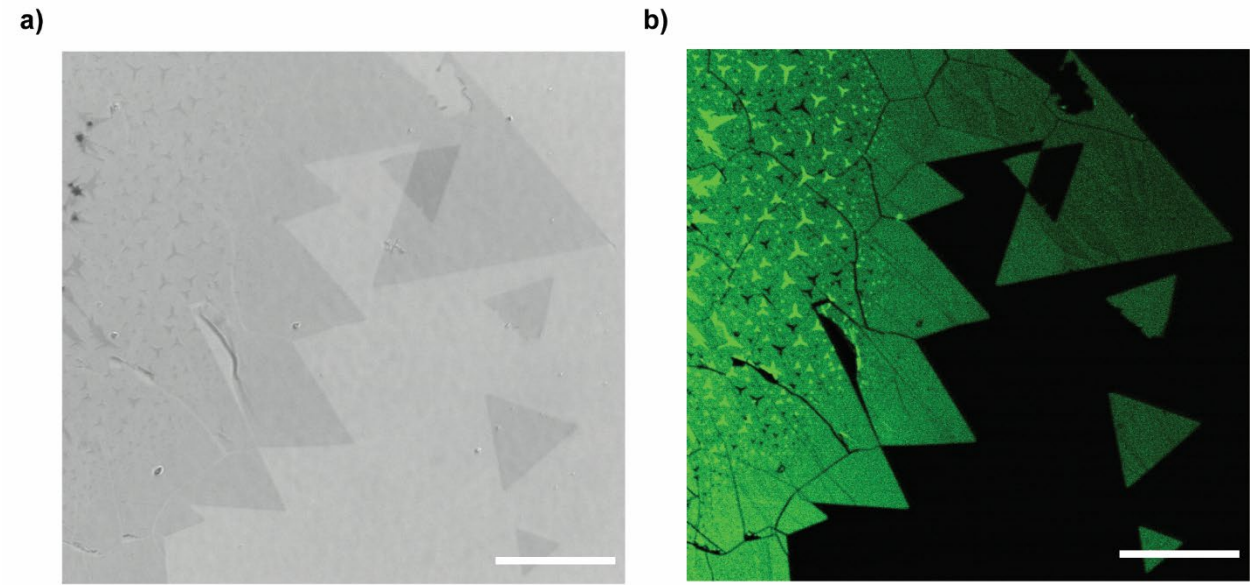

Figure S1. The optical microscopy image and (e) the corresponding SHG intensity map of the 2L-MoS_2 sample. The scale bars are 25 μm.

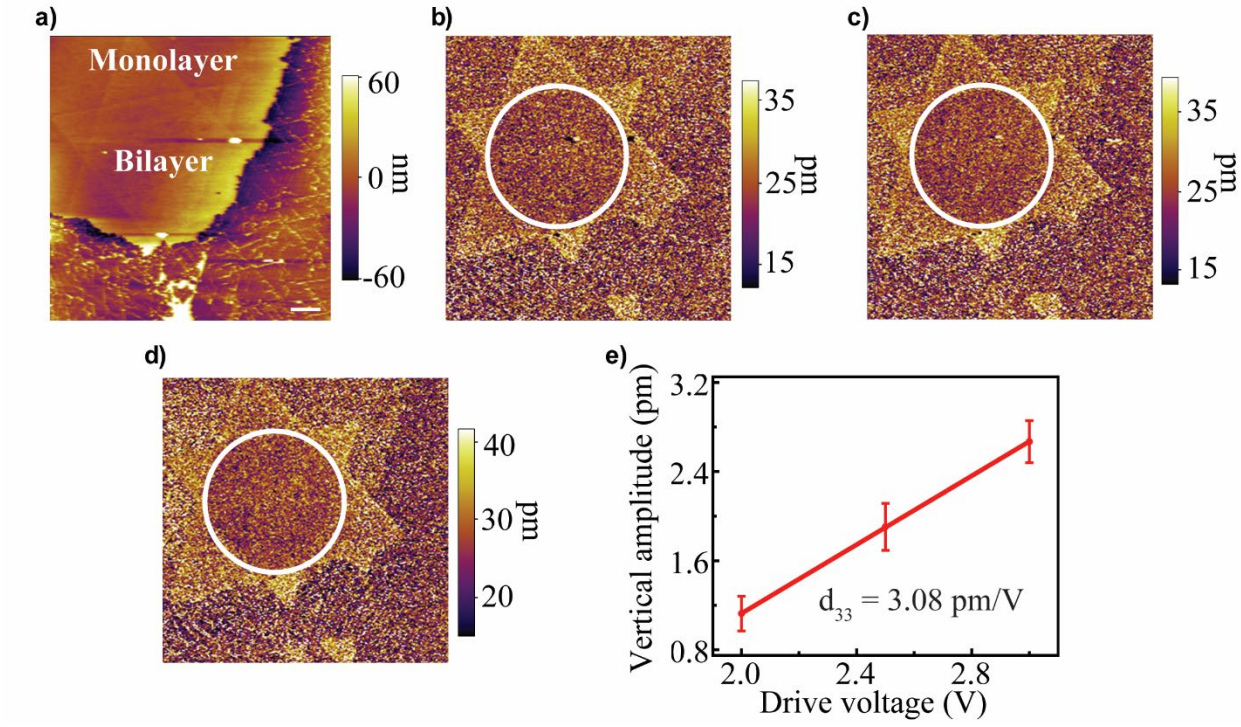

Figure S2. Out-of-plane piezoelectricity in the MoS_2 sample transferred on the flat conductive substate. (a) The AFM topography of the stacked 2L-MoS_2 sample transferred onto the flat substrate, and the corresponding vertical piezoresponses concerning different drive voltage of (b) 2.5 V, (c) 3V and (d) 3.5 V. (e) Average amplitude variations between the MoS_2 sample and the substrate as a function of applied voltages. The scale bars are 10 μm.

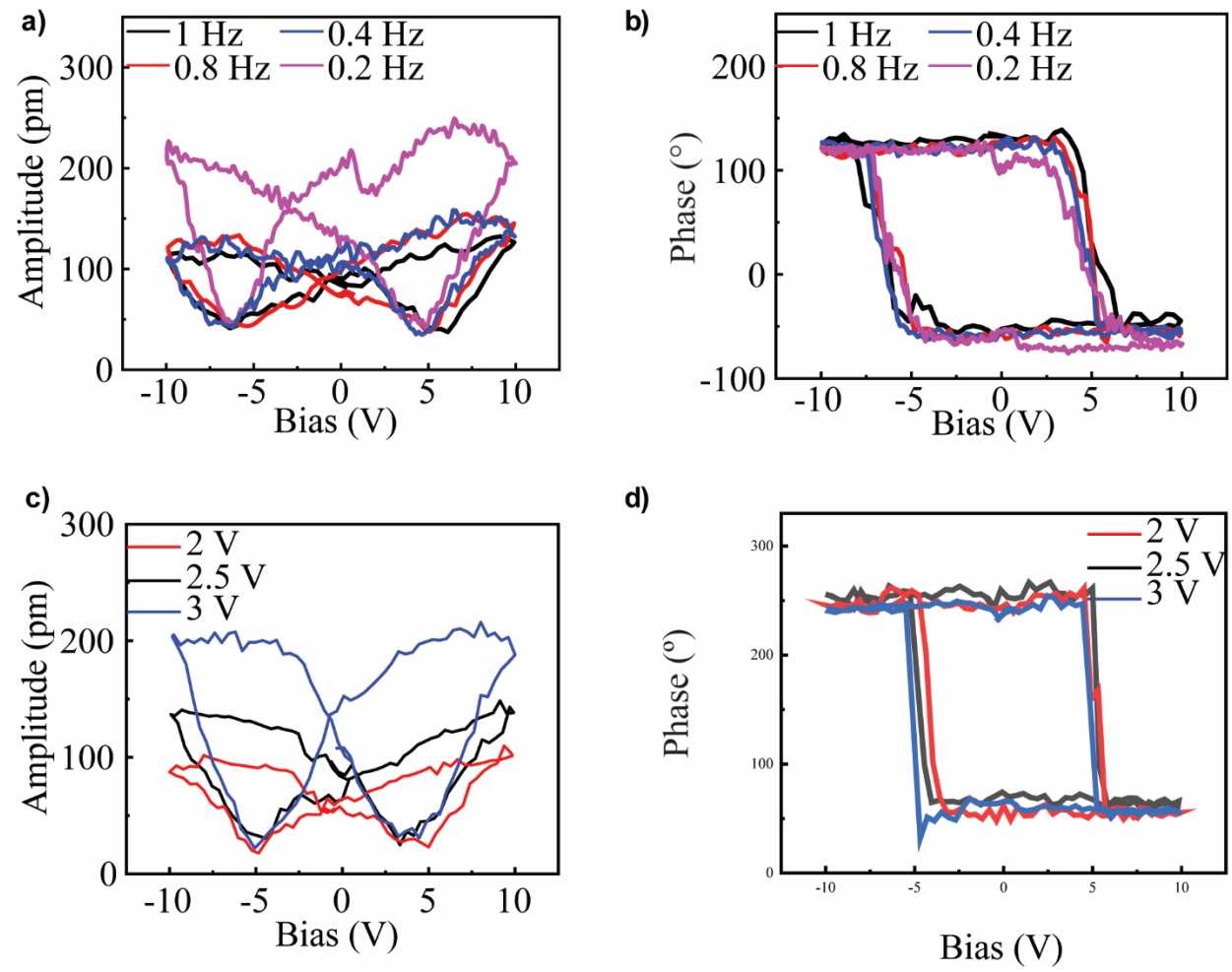

Figure S3. Piezoresponse hysteresis loops of the strained 2L-MoS_2 sample transferred on the nanocone substrate. PFM off-field (a) amplitude and (b) phase hysteresis loops at different frequency. PFM off-field (c) amplitude and (d) phase hysteresis loops at ac bias.

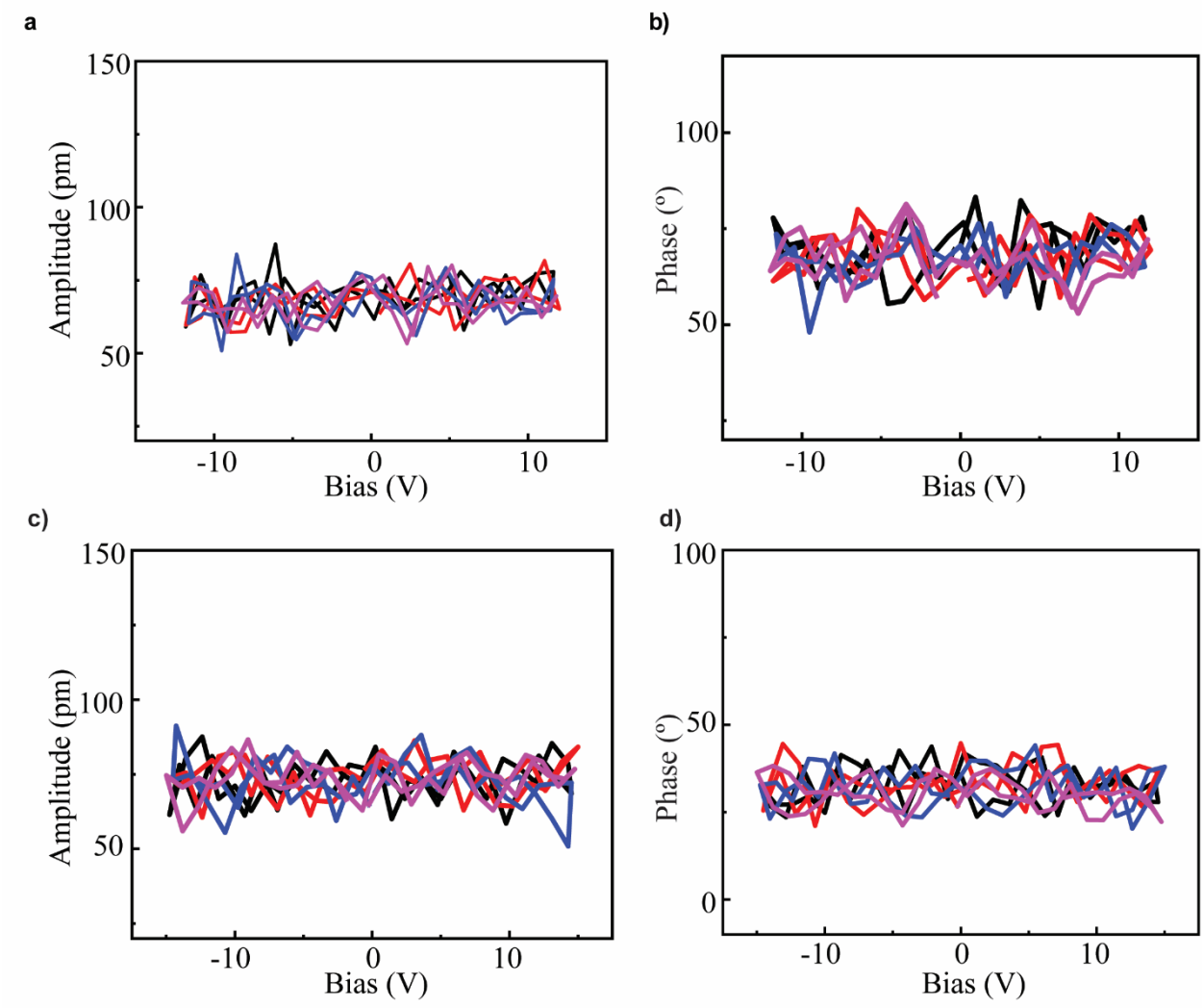

Figure S4. Piezoresponse hysteresis loops of the strained 1L-MoS_2 and unstrained 2L-MoS_2 samples. PFM off-field (a) amplitude and (b) phase hysteresis loops for 1L-MoS_2 at different positions. PFM off-field (c) amplitude and (d) phase hysteresis loops 2L-MoS_2 at different positions.

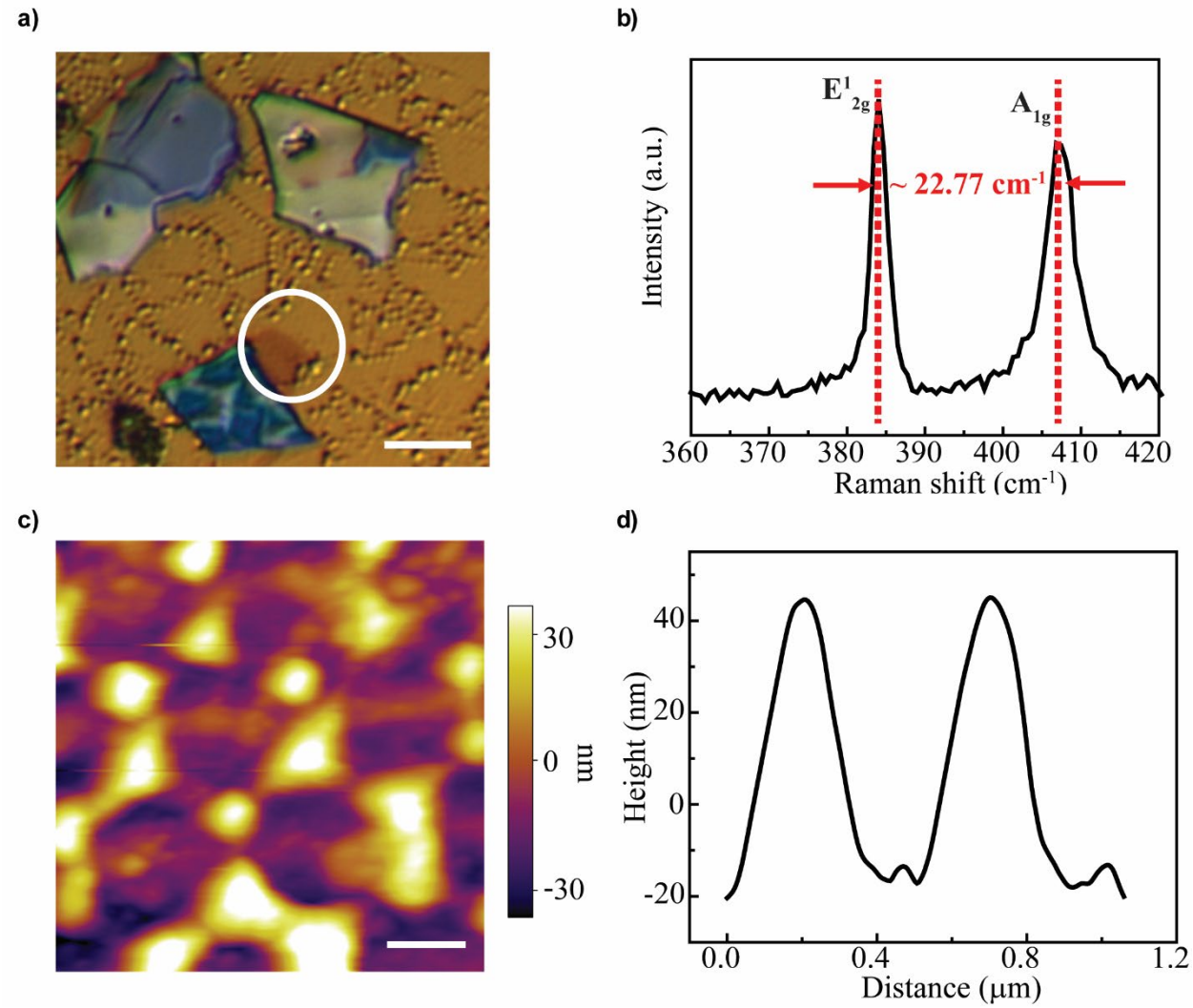

Figure S5. Strained 2L-MoS_2 sample exfoliated from the MoS_2 crystal. (a) The optical microscopy image of the exfoliated 2L-MoS_2 marked within a white circle. The scale bar is 10 μm. (b) Raman analysis of the exfoliated 2L-MoS_2 sample transferred on the nanocone substrate. (c) AFM topography of the exfoliated 2L-MoS_2 sample on the nanocone substrate and (d) the corresponding height analysis. The scale bar is 200 nm.

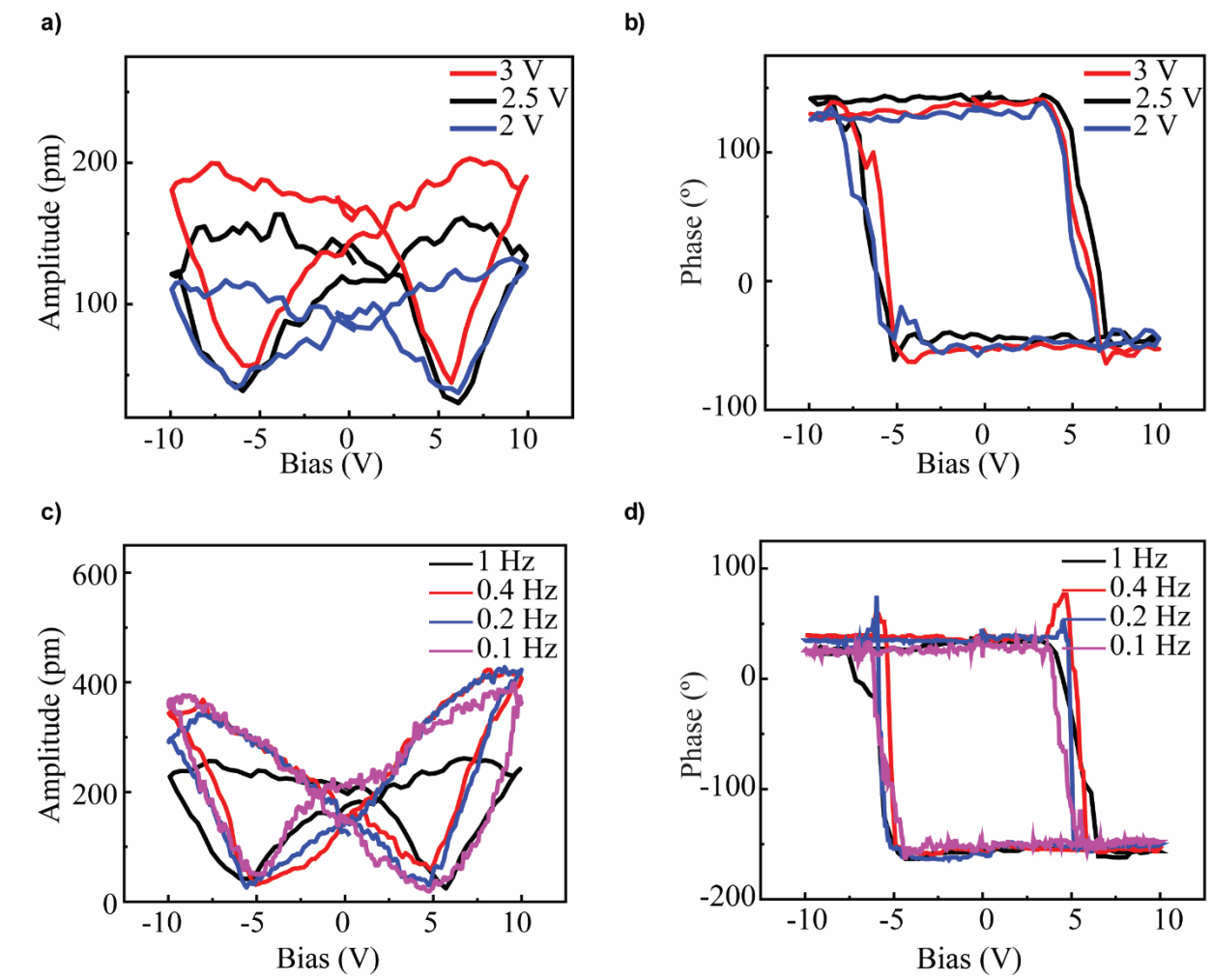

Figure S6. Ferroelectric switching of a strained 2L-MoS_2 sample exfoliated from the MoS_2 crystal. (a) PFM amplitude and (b) phase hysteresis loops for exfoliated 2L-MoS_2 with the DC field off at different ac bias. (c) PFM amplitude and (d) phase hysteresis loops for exfoliated 2L-MoS_2 with the DC field off at different scanning frequency.

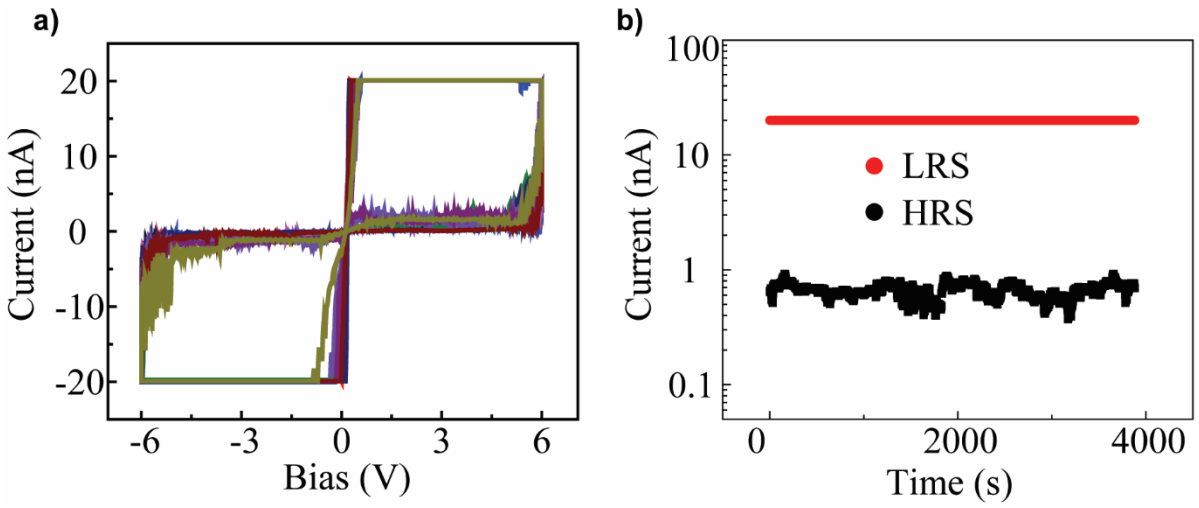

Figure S8. The *I-V* characteristics of the 2L-MoS_2 FTJ device after performing 10 cycles sweep voltage at room temperature. (b) The retention characteristics of the 2L-MoS_2 FTJ device.

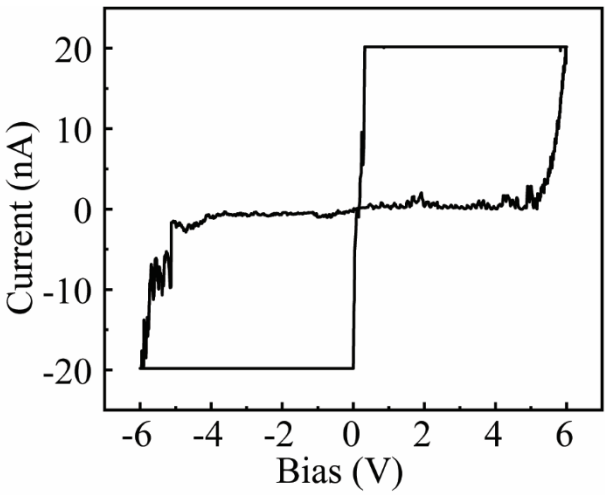

Figure S8. The *I-V* characteristics of the exfoliated 2L-MoS_2 FTJ device.

Table S1 Summary of piezoelectric coefficients from different materials.

Materials	d_{33}	Size	Ref
ZnO	12.4	bulk	[1]
GaN nanowires	12.8	64-191 nm	[2]
Bent InSe	19	11 nm	[3]
CdS	32.8	2-3 nm	[4]
α-In_2Se_3	5.6	bulk	[5]
$CuInP_2S_6$	10.2	0.72 nm (1 layer)	[6]
SnS_2	4.4	4 nm	[7]
Strained 1L-MoS_2	37.54	1 layer	This work
Strained 2L-MoS_2	24.8	2 layer	This work

REFERENCE

(1) Crisler, D.; Cupal, J.; Moore, A. Dielectric, piezoelectric, and electromechanical coupling constants of zinc oxide crystals. *Proc. IEEE* **1968**, *56* (2), 225-226. DOI: 10.1109/proc.1968.6246.

(2) Minary-Jolandan, M.; Bernal, R. A.; Kuljanishvili, I.; Parpoil, V.; Espinosa, H. D. Individual GaN nanowires exhibit strong piezoelectricity in 3D. *Nano Lett.* **2012**, *12* (2), 970-976. DOI: 10.1021/nl204043y.

(3) Wang, X.; Zhou, X.; Cui, A.; Deng, M.; Xu, X.; Xu, L.; Ye, Y.; Jiang, K.; Shang, L.; Zhu, L. Flexo-photoelectronic effect in n-type/p-type two-dimensional semiconductors and a deriving light-stimulated artificial synapse. *Mater. Horiz.* **2021**, *8* (7), 1985-1997. DOI: 10.1039/d1mh00024a.

(4) Wang, X.; He, X.; Zhu, H.; Sun, L.; Fu, W.; Wang, X.; Hoong, L. C.; Wang, H.; Zeng, Q.; Zhao, W. Subatomic deformation driven by vertical piezoelectricity from CdS ultrathin films. *Sci. Adv.* **2016**, *2* (7), e1600209. DOI: 10.1126/sciadv.1600209.

(5) Xue, F.; Zhang, J.; Hu, W.; Hsu, W. T.; Han, A.; Leung, S. F.; Huang, J. K.; Wan, Y.; Liu, S.; Zhang, J.; et al. Multidirection piezoelectricity in mono- and multilayered hexagonal α-In_2Se_3. *ACS Nano* **2018**, *12* (5), 4976-4983. DOI: 10.1021/acsnano.8b02152.

(6) Jiang, X.; Zhang, X.; Niu, R.; Ren, Q.; Chen, X.; Du, G.; Chen, Y.; Wang, X.; Tang, G.; Lu, J. Strong piezoelectricity and improved rectifier properties in mono-and multilayered $CuInP_2S_6$. *Adv. Funct. Mater.* **2023**, *33* (40), 2213561. DOI: 10.1002/adfm.202213561.

(7) Wang, Y.; Vu, L.-M.; Lu, T.; Xu, C.; Liu, Y.; Ou, J. Z.; Li, Y. Piezoelectric responses of mechanically exfoliated two-dimensional SnS_2 nanosheets. *ACS Appl. Mater. Interfaces*. **2020**, *12* (46), 51662-51668. DOI: 10.1021/acsami.0c16039.